Effects of body shape on aerodynamic performance and wake structures in snake-like gliding

Yuchen Gong¹, Junshi Wang², Wei Zhang³, Jake Socha⁴, and Haibo Dong⁵

 ^{1,2,3,5}Department of Mechanical and Aerospace Engineering, University of Virginia, Charlottesville, Virginia, 22904
 ⁴Department of Biomedical Engineering and Mechanics, Virginia Polytechnic Institute and State University, Blacksburg, VA 24061

Flying snakes are the only snakes on Earth capable of aerial gliding, taking advantage of fluid dynamic principles to leap from point to point among the trees. During their gliding, the locomotion of aerial undulation is observed. We hypothesize that this locomotion and its associated unsteady vortex dynamics are critical to their aerodynamic performance. However, there is a lack of detailed three-dimensional flow field information around the snake body in gliding due to the difficulties in experimental flow visualizations of live animals. In this study, a computation fluid dynamics (CFD) study has been conducted to study the fluid dynamics of a snake-like gliding. A mathematical equation describing the horizontal undulation motion was applied for constructing snake-like 3D computational models and a series of flow simulations were conducted. An immersed-boundary-method (IBM)-based direct numerical simulation (DNS) flow solver along with adaptive mesh refinement (AMR) was used in the simulation. Specifically, different head positions, corresponding to different horizontal wave shapes and their effect on aerodynamic performance, flow field and wake structures behind the body will be studied. In addition, the dynamic undulating motion is introduced in the model and a CFD simulation is also conducted. Results from this study are expected to bring a step stone to understanding snake-inspired locomotion.

Nomenclature

α	Angle of attack of the snake body
С	Chord length of snake body cross-section
C_L, C_D	Lift and drag force coefficient, respectively, of the snake body
κ	Curvature of the snake body
L	Length of snake body
Re	Reynolds numbers
s	Distance along the Snout-vent body length
S	Characteristic area of the snake body
U	Incoming flow velocity

¹ Ph.D. student, <u>vg6nc@virginia.edu</u>, AIAA student member.

² Ph.D. student, <u>iw9un@virginia.edu</u>, AIAA member. Now at Princeton University.

³ Postdoc, wz7ap@virginia.edu, AIAA member.

⁴ Professor, jjsocha@vt.edu.

⁵ Associate Professor, <u>hd6q@virgnia.edu</u>, AIAA Associate Fellow.

I. Introduction

In nature, lots of small animals' locomotion provided ideas for bio-inspired robots, such as swimming, flapping flight, walking and gliding. Flying snake (*Chrysopelea*), as a member of limbless reptiles, possesses the unique ability of gliding that no other species have. While aerial gliding, its body applies undulating motion and passes traveling waves down the body. The changing body shape will provide impact on the snake performance.

Over the past two decades, lots of research on the biomechanics of the gliding snake has been conducted to understand the flying snakes gliding, such as gliding trajectory [1] or 3-D kinematics analysis [2] with some qualitative analysis. Recently, Yeaton *et al.*[5] quantified a mathematical model describing the fundamental shape of the flying snake while gliding. A horizontal and a vertical undulating wave were identified which was also applied in this study as the inspiration of reconstruction of a series of 3-dimensional computational model.

There are also some experimental and numerical studies about the aerodynamic performance of the flying snake gliding. Most of them focused the configuration of the 2D cross-sectional shape of the snake, which appears to be a critical determinant in snake gliding. Experiment [3] applied a 2D snake-cross section model based on observed real snake cross-section to study how it affected the gliding performance. The angle of attack (α) and the Reynolds number (Re) were important parameters studied in the research. It was found out that the specific shape maximum lift at the angle of attack 35°. Based on that finding, a CFD simulation [4] studied the lift and wake with the same 2D cross-section shape. The study confirmed the conclusion with a peak lift generation at α =35°. The Reynolds number was investigated between 500 and 3000, which is lower than that in real world. Still, the CFD results provided some fundamental finding, including that the vortex structure formed at the near-wake helped enhancing the lift.

Despite the distinguished work done, there is still a huge knowledge gap between the current research progress and fully understanding the physics in undulation gliding and explaining the fluid dynamics mechanism beneath this specific locomotion. The aforementioned studies related to flying snakes either provided less fluid, or only limited to two-dimensional studies. No three-dimensional computational model with a body shape similar to natural posture has been studied. With the new mathematical model[5] and all those preliminary knowledge, we created a 3D snake body model and designed a series of cases to study its fluid physics.

In this paper, a starting case will be conducted on a static S-shaped snake body model with its head at initial position. A sharp-interface immersed-boundary-based direct numerical simulation solver is employed for the computational simulation. The purpose of this work is to examine the aerodynamic performance, such as lift, and the wake structure while the snake is gliding. Several snake models with different body shapes will be applied as comparison. Finally, one complete model with time-dependent horizontal undulation motion will be applied and its results will be compared with the static cases.

II. Methodology

A. 3D flying snake model kinematics

The current work employs the new mathematical model of limbless flight generated from previous study done by Yeaton[5]. By applying the 'aerial serpenoid curve', the horizontal waves are modeled with the following equations:

$$\bar{\theta}(s,t) = \theta_{max} \sin\left[\frac{\pi}{2}\cos\left(\frac{2\pi\nu_{\theta}}{L}s - 2\pi ft\right)\right] \tag{1}$$

More details about the mathematical model can be discovered in Ref [1].

Figure 1(b) shows one of the models generated with a set of specific parameters: $\theta_{max} = 93^{\circ}$, $\nu_{\theta} = 1.4$, f = 1, t/T = 0 (T = 1/f). The maximum horizontal bending angle θ_m and spatial period number ν_{θ} is a set of parameters observed in real flying snake gliding experiments. The curvature κ of the snake is also defined with the osculating circle of the midline curve. This concept is used for the discussion of different snake shapes.

The equation and parameters describing vertical bending is not introduced in this study so that the effect of the pure horizontal body shape can be studied. Figure (c) shows no vertical (in Y direction) deformation. This steady shape is set up as starting case (Case 0) in our simulation.

In Figure 1(d) the cross-section shape of the flying snake body was showed. It was originated from high speed video and also applied in previous experiment and numerical study [2-3]. Its chord length is defined as C and the body length is also defined as L = 35c. This body-chord ratio is measured from the video [2].

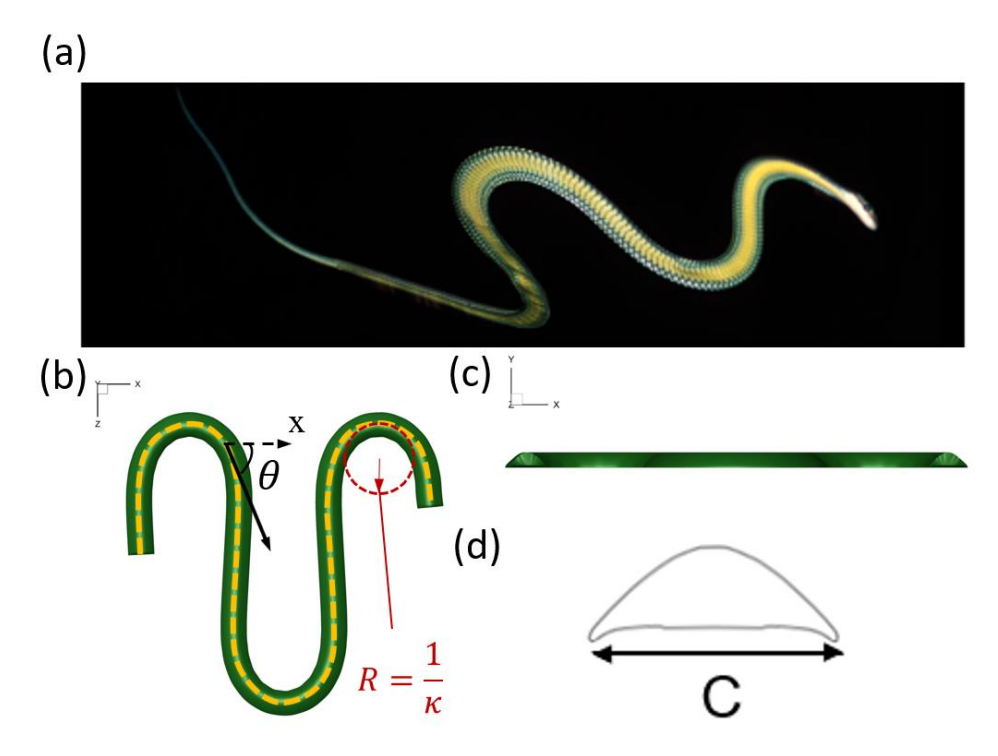


Figure 1: (a) Body wave shape of flying snake *Chrysopelea paradisi* in ventral view [2]; (b) Top view of the reconstructed 3D model using the math equation; (c) Side view of the model; (d)Cross-sectional geometry applied in snake body model [2]

To further study the effect of snake wave shape, a phase shift is introduced through changing different time t. Given the symmetry of the wave function, only first half of the undulation motion is adopted to create different static shapes models with t/T=0.1,0.2,0.3,0.4. The corresponding phase change will be $-0.2\pi,-0.4\pi,-0.6\pi,-0.8\pi$ as shown in Figure 2 (a)-(d) (As our Case 1 to 4). Finally, we created time-variant dynamic model based on the equation and conducted the simulation with horizontal undulating motion (Case 5). Table 1 summarized the case setup with different t.

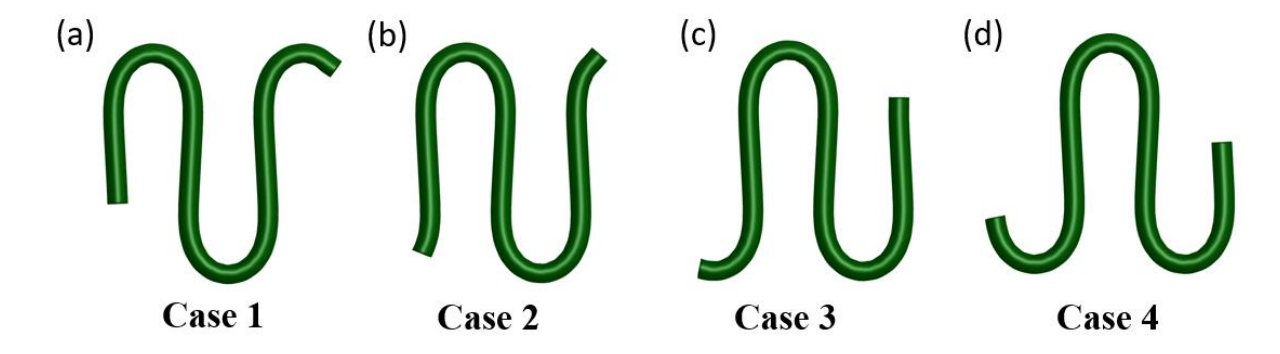


Figure. 2 Static cases with different wave shapes corresponding to time at t/T=0.1, 0.2, 0.3 and 0.4.

Table 1. Case Setup

	Static	Static	Static	Static	Static	Dynamic
	Case 0	Case 1	Case 2	Case 3	Case 4	Case 5
t	0	0.1	0.2	0.3	0.4	/

B. Numerical method and simulation setup

The governing equations solved in this work are the incompressible Navier-Stokes equations, written in indicial form as,

$$\frac{\partial u_i}{\partial x_i} = 0; \quad \frac{\partial u_i}{\partial t} + \frac{\partial u_i u_j}{\partial x_i} = -\frac{\partial p}{\partial x_i} + \frac{1}{Re} \frac{\partial^2 u_i}{\partial x_i \partial x_j}$$
 (2)

where u_i are the velocity components, p is the pressure, and Re is the Reynolds number. The equations are nondimensionalized with the appropriate length and velocity scales.

An in-house finite-difference based Cartesian-grid sharp-interface immersed-boundary-method direct numerical simulation solver [6] is employed to solve the equations above. This approach has been successfully applied to the flapping propulsion of insects [7-9], birds [10,11] fish [12-14], as well as various canonical problems such as fish schooling, hovering flight, uvula flapping and so on [15-19]. Detailed description of the sharp-interface method and validation of this solver can be found in Ref. [20-22].

In this study, the non-dimensional parameters of Reynolds number Re is defined as follows,

$$Re = \frac{UC}{v},\tag{3}$$

where U denotes the incoming flow velocity, ν denotes the kinematic viscosity of the flow, C stands for the characteristic length of the cross-section of the body. In real world, the Reynolds number is within the range of 5000-15000[1].

Table 2. Summary of important parameters in this study

U	Re	α	θ_m	$\nu_{ heta}$	f
20	500	35°	93°	1.4	1

The computational domain has the dimension of $200C \times 200C \times 200C$. A Cartesian grid configuration with stretching grid is employed in the current study. The spacing of the cell in 3 directions within the densest region is $\Delta = 0.04C$, which is proven to be fine enough for the present simulation. To apply adaptive mesh refinement (AMR) techniques, a block-structured-mesh were designed to improve the quality of mesh. A larger parent block was introduced to capture the main flow structure at far field and a smaller block was introduced to be set close to computational model to focus on the near field characteristics. The left and the bottom boundaries are set as velocity inlet with constant incoming flow velocity $U\cos\alpha$ and $U\sin\alpha$. In the baseline case, the angle of attack α of the flow is set to be 35° since it's where the maximum lift coefficient is generated according to experiment and CFD simulation data. The zero-gradient boundary condition is applied to the right boundary to allow the convection of the vortices without significant reflection. The zero-stress boundary condition is provided at all vertical boundaries. A homogeneous Neumann boundary condition is used for the pressure at all boundaries. No-slip boundary condition is applied at the plate surface.

In Figure 3 a schematic computational grid with multiple AMR blocks were shown. Detailed analysis about the AMR algorithm can be seen in Ref [23].

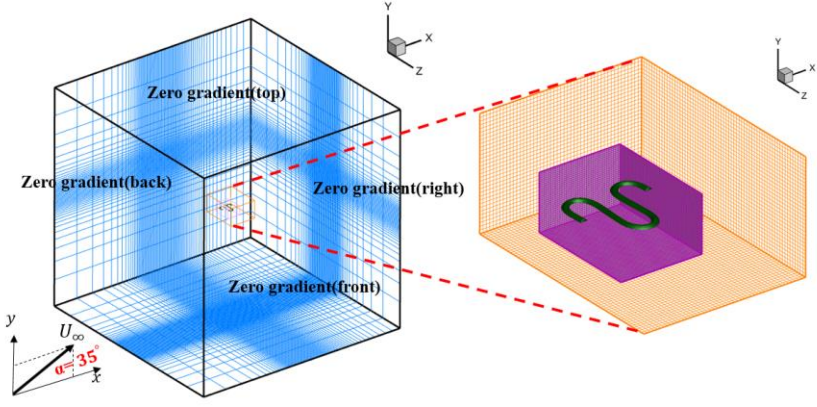


Fig. 3 Schematics of the computational grids with AMR blocks

The lift coefficient C_L , drag coefficient C_D , are defined to quantify the performance of the flexible plate as follows,

$$C_L = \frac{Lift}{\frac{1}{2}\rho U^2 S}, \qquad C_D = \frac{Drag}{\frac{1}{2}\rho U^2 S}$$

$$\tag{4}$$

where S denotes the planform area of the plate with S = Lc.

The definition of Lift and Drag is the force perpendicular to or in line with to the flow direction. In the computational domain, the x and y direction force, F_x and F_y , were calculated by integrating the force along the surface body. Then we decompose the force into lift and drag direction with Equation 5 and 6. Finally, we obtain the force coefficient with equation 4 mentioned above.

$$Lift = F_{v}\cos(\alpha) - F_{x}\sin(\alpha) \tag{5}$$

$$Drag = F_x \cos(\alpha) + F_y \sin(\alpha) \tag{6}$$

III. Results and Discussion

In this section, the flying-snake 3D model is studied with several different static wave shape profiles. To start with, the aerodynamics performance, surface pressure results and three-dimensional vortex structures of the baseline model is analyzed compared. Next, we study the effects of the wave shapes by choosing several different timeframes' static snake posture. Finally, one complete horizontal undulating gliding snake model is also investigated and some fundamental comparison are made with static cases.

A. Aerodynamic performances

Figure 3Figure shows the instantaneous lift and drag coefficient on the starting case 0. To reach steady state, the force history is shown between non-dimensional time t = 140-160. Normalized time t^* is calculated with freestream velocity U and chord length $c(t^* = tU/c)$. Time-averaged force coefficient is also calculated between this time period to eliminate the initial condition. From the time history we can observe the oscillation caused by vortex shedding and regeneration process on the surface, which will be discussed in later section.

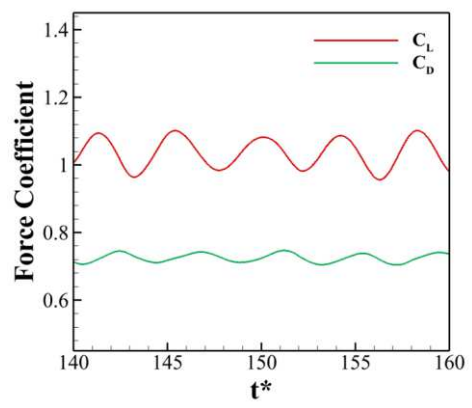


Figure 4: The instantaneous lift coefficient on the flying snake at non-dimensional time 140 to 160. B. Vortex structure near the body

Figure 5 illustrates the vortex structure around and at the wake of the computational model in gliding. The snapshot of the vortex is taken at a local lift peak. The iso-surface structures are visualized using Q-criterion with the value of 200. The main feature on the body can be identified is the edge vortices (EV) generated on the straight part of the body. Topologically speaking, the straight tube is the hint of 2D leading-edge vortices (LEV) expanding it spanwise (the third dimension in space). Similarly trailing-edge vortex tubes (TEV) can also be observed below the LEV. Interaction between each plane may merge into different structures such as hairpin vortices. Similar process and structure were investigated and reported in three-dimensional flow around a flat plate by Taira *et al* [24], especially with larger aspect ratio.

Tip vortex (TV) is also a prominent vortex structure observed at the head. The blue contoured, counter-clockwise rotating TV shares the similar vortex loop structure at the head (tip) similar as the simulation done by Taira *et al* [24] with low-aspect-ratio wings or Li *et al*.[25] with revolving wing.

One unique vortex structure observed in the current snake is the side (edge) vortices (SV). SVs are generated on the turning curved part of the snake body. They share some similar topology shape as the TV, since they are all formed on the edge of the model. But SV is more complicated than the TV. Due to the turning of the body, this particular section can be treated as a wing with span-wise flow only. The flow passes along both leading and trailing edges with

a velocity perpendicular to the cross-section. The spinning vortex loop pairs with curved shape comes from the vortex loops generated on both sides of the body and merged together. EV, TV and SV are formed on different parts of the snake model, interacting with each other all the time, contributing to a complicated wake topology.

Figure 5 (b) **Figure** shows vortex structures near the body the flying snake. From the figure, the main feature that can be identified is the vortex structure on the straight body. A pair of blue clockwise LEV and red counter-clockwise TEV are experiencing the shedding from the dorsal and ventral surface. This shows similar process as in 2D simulation conducted by Krishnan *et. al* [3]. The hints of TV and SV can also be identified as a stretched region in the figure.

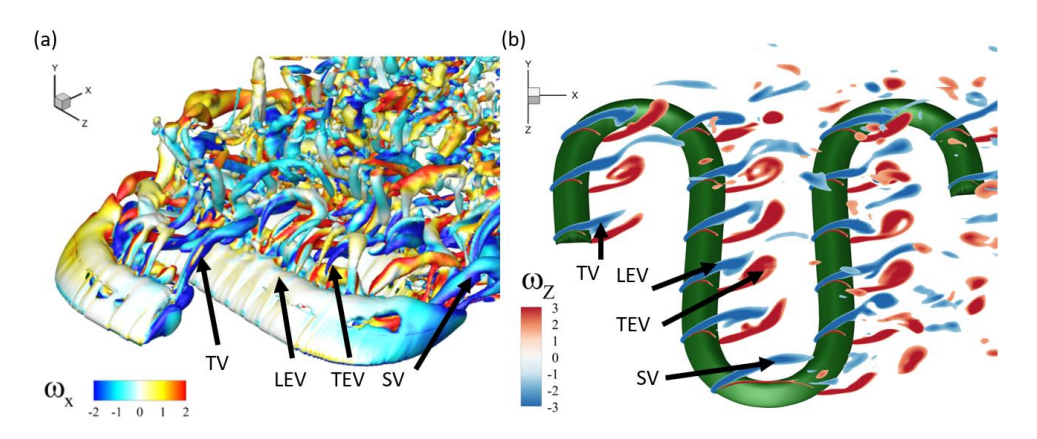


Figure 5: (a)Perspective view of wake structure of the baseline case at peak lift distribution. The iso-surfaces are plotted using Q-criterion with Q=200 and flooded by X-vorticity ω_X ; (b) Vortex structure near the snake body at peak lift distribution. Z-vorticity ω_Z is applied to visualize the vortices on six slices cutting through the body. ω_X and ω_Z are all normalized by U/c.

C. Surface pressure

LEV and TEV are observed on the body of the snake. The existence of LEV and TEV will produce low pressure and high pressure correspondingly, providing a pressure difference along the whole body. The total resultant force contributes to the lift generation. Figure 6 (a) shows the pressure coefficient difference between the dorsal and ventral surface of the body. On the leading edge of the dorsal surface, a relatively darker high-pressure-difference ΔC_P region indicates the leading-edge vortices. The contour also corresponds with Figure 6(b), which illustrates the lift distribution C_L along the body. The high-pressure region generates higher lift, which is shown with deep red zones on the leading edge. The green zones are more commonly observed at head, tip and turning body, indicating that TV and SV contribute less to lift generation.

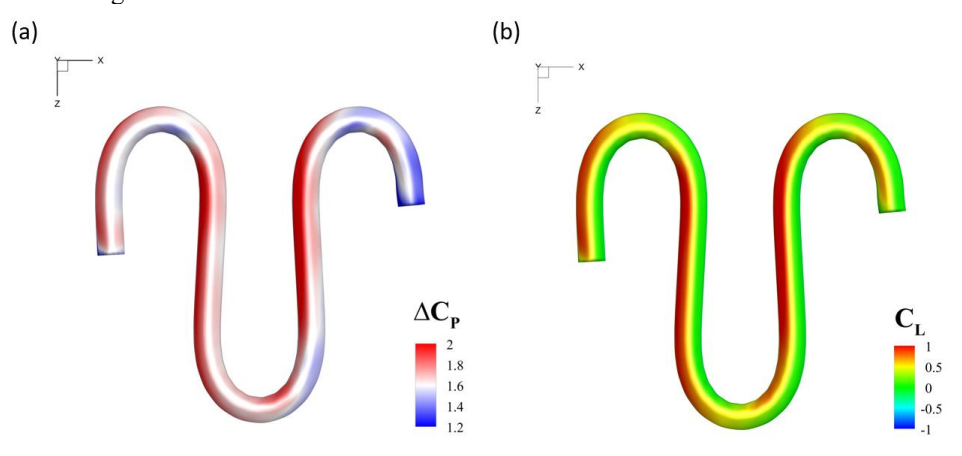


Figure 6: (a) Pressure difference (ΔC_P) between dorsal and ventral surface;(b) Lift coefficient (C_L) distribution along the body

D. Effect of body shapes

In this section, the results of different body shapes are discussed. Figure 7 shows the result of cycle averaged lift coefficient. From the curve it is observed that with the body shape at Case 2 provides the maximum lift in gliding.

In order to explain the effect of body shape, the curvature κ of the midline on the snake model is calculated. By defining the curved body as where curvature greater than 0.2 ($\kappa \ge 0.2$), we can summarize a general trend that the body shape with less curved body provides higher lift. The detailed data can be obtained in Table 3.

To further validate our hypothesis, figure 8 compares the difference between Case 2, which possess the maximum lift and minimum curved body (41.3%), and Case 3, which provides 2.8% less lift with a head at the U turning leading to longer curved body (45.7%). To explain the lift difference, we investigated the wake structures of the two cases in figure 8 (a) and (b). In Case 2, the long straight body generates a LEV tube on the dorsal surface, which makes significant contribution to the lift generation. The body shape of Case 3 is in a special position since the head is making the turning, so that the tip (head) vortex TV can also be merged with side edge vortex (SV). Either vortex provides less lift than the straight LEV. The hypothesis can be further validated from the lift distribution contour in Figure 8 (c) and (d). In both cases, straight body with steady LEV tubes possesses larger red region, providing higher lift. The head in case 2 which is perpendicular to incoming flow in Case 2 becomes parallel to x flow in Case 3. Thus, the red region on the head turns green, showing less lift distribution.

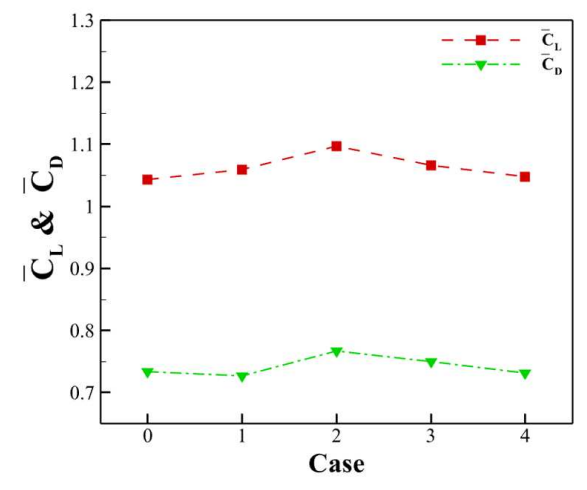


Figure 7: Time-averaged lift(C_L) and drag(C_D) coefficient of different cases.

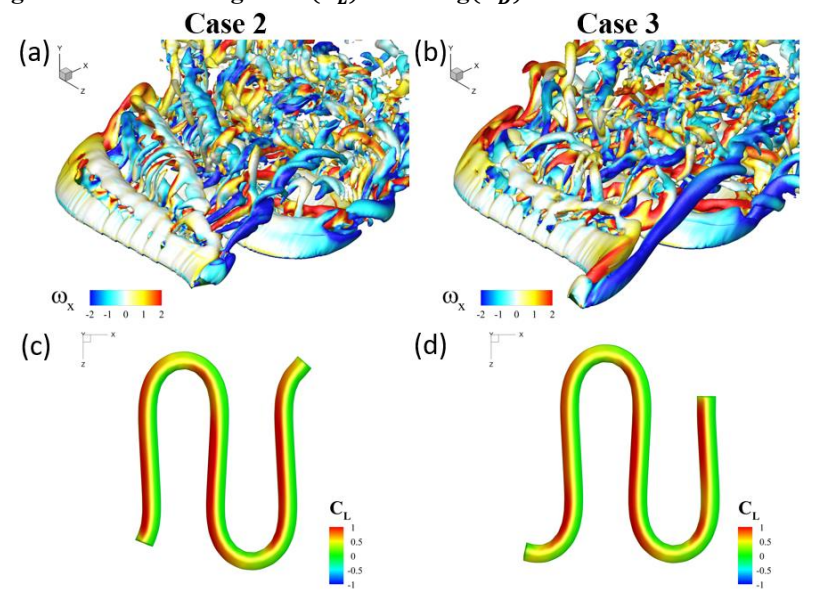


Figure 8: (a) and (b) show the perspective view of wake structure of Case 2 and 3 at peak lift timeframe; (c) and (d) show the lift coefficient (C_L) distribution along the body of the two cases, respectively.

Case	0	1	2	3	4
$\overline{C_L}$	1.0436	1.0588	1.0968	1.0657	1.0482
$\overline{C_D}$	0.7332	0.7267	0.7672	0.7500	0.7311
Curved Body Portion $(\kappa \ge 0.2)$	51.1%	45.7%	41.3%	45.7%	52.2%

Table 3. Summary of important parameters in this study

E. Effect of the motion of horizontal undulation

In the final section, we investigate the aerodynamics of the dynamic snake model. By applying undulation frequency f=1, the moving model was created and the simulation was conducted. In Figure 9(a), the simulation result for lift coefficient is shown after 4 undulation cycles so that the flow field is in a steady periodic condition. It's found that the instantaneous force history is symmetric in the right-to-left and left-to-right cycles due to the prescribed symmetric motion. The results in moving Case 5 are quite different those from steady cases. For the two dashed line points t/T=0.2 and 0.3, which possess the same body shape as Case 2 and 3, $C_L \left(t/T = 0.2 \right) = 0.8897$ is smaller than $C_L \left(t/T = 0.3 \right) = 1.0117$. The result is different from that in static cases

The different phenomenon results from the introduction of horizontal undulating motion. Figure 9 (b) and (c) show the vortex wake of the model at t/T=0.2 and 0.3. The basic vortex structure is similar as the steady snake model with TV at head, LEV and TEV on the straight body and SV near the turning body. However, the introduction of motion will provide spanwise velocity on the straight body. The LEV tube parallel to the body and the TV parallel to flow direction are all stretched into oblique vortex tubes pointing into Z direction. The deformation of vortex tubes will lead to different lift generation profile. In the future there will be more detailed analysis based on the dynamic motion models.

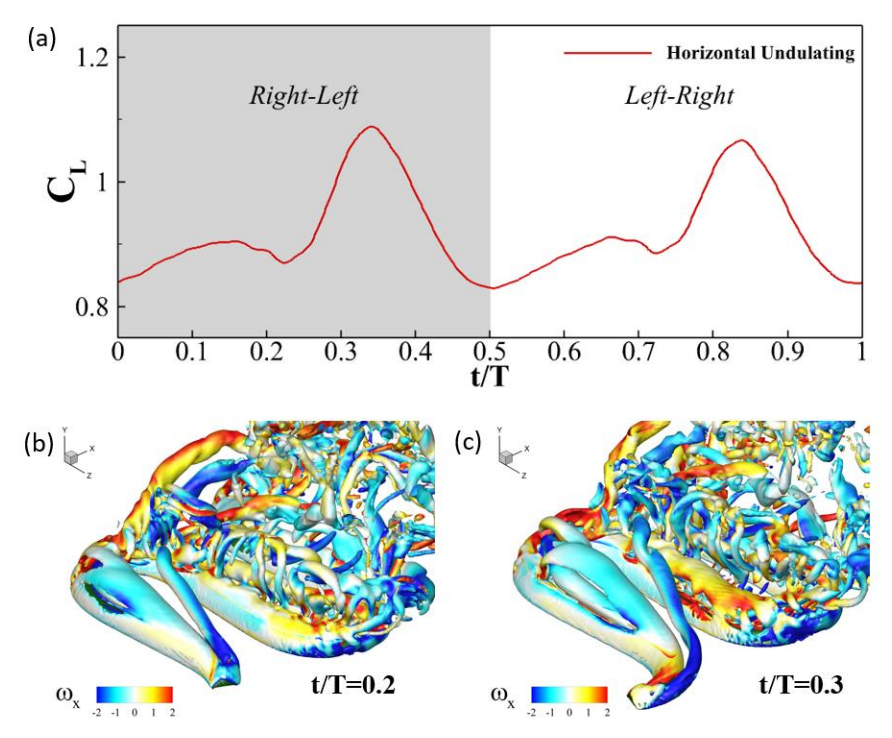


Figure 9: (a) The instantaneous lift coefficient on the flying snake with in one complete horizontal undulation period. The force history shows symmetrical pattern; (b) and (c) show the wake structure at t/T=0.2 and 0.3, which corresponds with the shape in Case 2 and 3.

IV. Conclusion

In this study, a computation study of various body shapes in a three-dimensional flying snake model has been conducted by using an in-house immersed-boundary-method based numerical solver. Five different body shapes are employed in the study to investigate their effects on aerodynamic performance and wake structures during gliding. The aerodynamic performance shows similar pattern as 2D cross-section shape with vortex shedding. The major vortex structures identified near the snake body are tip vortex (TV), leading-edge and trailing-edge vortices (LEV and TEV) and side edge vortex (SV). Among them, LEV plays the dominant role in lift enhancement. This also leads to the effect of changing snake body shape on aerodynamic performance. The shape with shorter curved body and longer straight body will generate longer LEV tubes, which improves lift generation.

Further analysis on a dynamic gliding snake model shows different results from steady snake models. With the constant changing of snake body shape due to the undulating, the aerodynamic performance shows periodic change along with the motion. The vortex structures near the body also changes significantly due to the motion in Z direction.

Acknowledgments

This research is supported by NSF grant CBET-2027534 and ***.

References

- [1] Socha, J. J., O'Dempsey, T., & LaBarbera, M. (2005). A 3-D kinematic analysis of gliding in a flying snake, Chrysopelea paradisi. Journal of Experimental Biology, 208(10), 1817–1833. https://doi.org/10.1242/jeb.01579
- [2] Socha, J. J., Miklasz, K., Jafari, F., & Vlachos, P. P. (2011). Erratum: Non-equilibrium trajectory dynamics and the kinematics of gliding in a flying snake (Bioinspir. Biomim. (2010) 5 (045002). In Bioinspiration and Biomimetics (Vol. 6, Issue 1). https://doi.org/10.1088/1748-3182/6/1/019501
- [3]Holden, D., Socha, J., Cardwell, N., and Vlachos, P., "Aerodynamics of the flying snake Chrysopelea paradisi: how a bluff body cross-sectional shape contributes to gliding performance", Journal of Experimental Biology, Vol. 217, No. 3, 2014, pp. 382-394.
- [4] Krishnan, A., Socha, J., Vlachos, P., and Barba, L., "Lift and wakes of flying snakes", Physics of Fluids, Vol. 26, No. 3, 2014, p. 031901.
- [5]Yeaton, I., Ross, S., Baumgardner, G., and Socha, J., "Undulation enables gliding in flying snakes", Nature Physics, Vol. 16, No. 9, 2020, pp. 974-982.
- [6] Mittal, R., Dong, H., Bozkurttas, M., Najjar, F., Vargas, A., and von Loebbecke, A., 2008, "A versatile sharp interface immersed boundary method for incompressible flows with complex boundaries," Journal of computational physics, 227(10), pp. 4825-4852.
- [7] Dong, H., C. Koehler, Z. Liang, H. Wan, and Z. Gaston (2010). "An Integrated Analysis of a Dragonfly in Free Flight". 40th AIAA Fluid Dynamics Conference and Exhibit, AIAA-2010-4390.
- [8] A. Bode-Oke, S. Zeyghami and H. Dong, Aerodynamics and flow features of a damselfly in takeoff flight, Bioinspiration & Biomimetics, 12(5), 056006, 2017.
- [9] Bode-Oke, A. T., Zeyghami, S., and Dong, H., 2018, "Flying in reverse: kinematics and aerodynamics of a dragonfly in backward free flight," Journal of The Royal Society Interface, 15(143).
- [10] Ren, Y., Dong, H., Deng, X., and Tobalske, B., 2016, "Turning on a dime: Asymmetric vortex formation in hummingbird maneuvering flight," Physical Review Fluids, 1(5), p. 050511.
- [11] Wang, J., Ren, Y., Li, C., and Dong, H., 2019, "Computational investigation of wing-body interaction and its lift enhancement effect in hummingbird forward flight," Bioinspiration & Biomimetics, 14(4), p. 046010.
- [12] Liu, G., Ren, Y., Dong, H., Akanyeti, O., Liao, J. C., and Lauder, G. V., 2017, "Computational analysis of vortex dynamics and performance enhancement due to body-fin and fin-fin interactions in fish-like locomotion," Journal of Fluid Mechanics, 829, pp. 65-88.
- [13] Han, P., Lauder, G., and Dong, H., "Hydrodynamics of median-fin interactions in fish-like locomotion: Effects of fin shape and movement", Physics of Fluids, Vol. 32, No. 1, 2020, p. 011902
- [14]Wang, J., Wainwright, D. K., Lindengren, R. E., Lauder, G. V., and Dong, H., 2020, "Tuna locomotion: a computational hydrodynamic analysis of finlet function," Journal of The Royal Society Interface, 17(165), p. 20190590.
- [15] Pan, Y., & Dong, H. (2020). Computational analysis of hydrodynamic interactions in a high-density fish school. Physics of Fluids, 32(12).

- [16] Werner, N. H., Chung, H., Wang, J., Liu, G., Cimbala, J. M., Dong, H., and Cheng, B., 2019, "Radial planetary vorticity tilting in the leading-edge vortex of revolving wings," Physics of Fluids, 31(4), p. 041902.
- [17] Dong, H., Z. Liang and M. Harff, Optimal Settings of Aerodynamic Performance Parameters in Hovering Flight, International Journal of Micro Air Vehicle, Vol.1, Number 3, pp 173-181, 2009.
- [18]H. Dong and Z. Liang, "Effects of Ipsilateral Wing-Wing Interactions on Aerodynamic Performance of Flapping Wings", Proceeding of 48th AIAA Aerospace Sciences Meeting and Exhibit with New Horizons Forum, AIAA paper 2010-0071.
- [19] Wang, J., Xi, J., Han, P., Wongwiset, N., Pontius, J., and Dong, H., "Computational analysis of a flapping uvula on aerodynamics and pharyngeal wall collapsibility in sleep apnea", Journal of Biomechanics, Vol. 94, 2019, pp. 88-98
- [20] Chang, C.-H., Deng, X., and Theofanous, T. G., 2013, "Direct numerical simulation of interfacial instabilities: a consistent, conservative, all-speed, sharp-interface method," Journal of Computational Physics, 242, pp. 946-990.
- [21] Dong, H., Mittal, R., and Najjar, F. M., 2006, "Wake topology and hydrodynamic performance of low-aspectratio flapping foils," Journal of Fluid Mechanics, 566, pp. 309-343.
- [22] Narasimhan, M., H. Dong, R. Mittal, and S. Singh, "Optimal Yaw Regulation and Trajectory Control of Biorobotic AUV Using Pectoral Fins Based on CFD Parameterization", Journal of Fluids Engineering, 128(2006), 687-698.
- [23] Zhang, W., Pan, Y., Gong, Y., Dong, H., & Xi, J. (2021, August). A Versatile IBM-Based AMR Method for Studying Human Snoring. In Fluids Engineering Division Summer Meeting (Vol. 85284, p. V001T02A039). American Society of Mechanical Engineers.
- [24] Taira, K., & Colonius, T. (2009). Three-dimensional flows around low-aspect-ratio flat-plate wings at low Reynolds numbers. Journal of Fluid Mechanics, 623, 187–207.
- [25]Li, C., Dong, H., & Cheng, B. (2020). Tip vortices formation and evolution of rotating wings at low Reynolds numbers. Physics of Fluids, 32(2).